

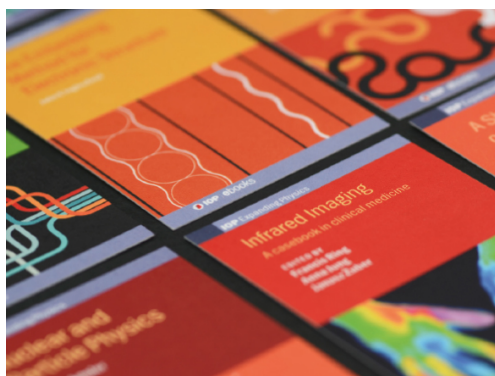
Hydration properties of mechanosensitive channel pores define the energetics of gating

To cite this article: A Anishkin *et al* 2010 *J. Phys.: Condens. Matter* **22** 454120

View the [article online](#) for updates and enhancements.

You may also like

- [Physically based principles of cell adhesion mechanosensitivity in tissues](#)
Benoit Ladoux and Alice Nicolas
- [Dynamic regulation of mechanosensitive channels: capacitance used to monitor patch tension in real time](#)
Thomas M Suchyna, Steven R Besch and Frederick Sachs
- [A skin-inspired soft material with directional mechanosensation](#)
Michelle M Makhoul-Mansour, Elio J Challita, Adarsh Chaurasia et al.



IOP | ebooks™

Bringing together innovative digital publishing with leading authors from the global scientific community.

Start exploring the collection—download the first chapter of every title for free.

Hydration properties of mechanosensitive channel pores define the energetics of gating

A Anishkin, B Akitake, K Kamaraju, C-S Chiang and S Sukharev

Department of Biology, University of Maryland, College Park, MD 20742, USA

E-mail: sukharev@umd.edu

Received 16 April 2010, in final form 12 July 2010

Published 29 October 2010

Online at stacks.iop.org/JPhysCM/22/454120

Abstract

Opening of ion channels directly by tension in the surrounding membrane appears to be the most ancient and simple mechanism of gating. Bacterial mechanosensitive channels MscL and MscS are the best-studied tension-gated nanopores, yet the key physical factors that define their gating are still hotly debated. Here we present estimations, simulations and experimental results showing that hydration of the pore might be one of the major parameters defining the thermodynamics and kinetics of mechanosensitive channel gating. We associate closing of channel pores with complete dehydration of the hydrophobic gate (occlusion by ‘vapor lock’) and formation of two water–vapor interfaces above and below the constriction. The opening path is the expansion of these interfaces, ultimately leading to wetting of the hydrophobic pore, which does not appear to be the exact reverse of the closing path, thus producing hysteresis. We discuss specifically the role of polar groups (glycines) buried in narrow closed conformations but exposed in the open states that change the wetting characteristics of the pore lining and stabilize conductive states of the channels.

(Some figures in this article are in colour only in the electronic version)

1. Introduction

Instability of water layers on hydrophobic surfaces known from the time of Young and Laplace [1] as dewetting has many natural manifestations and practical applications [2]. While super-hydrophobic feathers or furs extend animal habitats to inhospitable climates, the hydrophobic effect acting at a molecular scale drives phase separation in chemical processes and assembly of cellular components [3]. Directionality and cooperativity of hydrogen bonds make interfacial water somewhat different from bulk water [4–6] and these unusual properties make it very special for biology [7].

Any process of assembly or cohesion in an aqueous phase involves expulsion of the thin layer of water between the surfaces, which becomes less stable as it gets thinner. Formation of a low-density layer of water near hydrophobic surfaces was predicted theoretically [8] and supported experimentally [9]. Spontaneous formation of vapor bubbles on fully submerged flat hydrophobic surfaces was demonstrated with atomic force microscopy [10]. Instability

of liquid water in a narrow hydrophobic confinement, known as capillary evaporation, was simulated in slits between planar apolar surfaces [11] as well as in nanotubes [12] and the probability and kinetics of dewetting was shown to be critically dependent on the strength of water–wall interactions. In many instances formation of vapor cavities in hydrophobic confinement was found to be thermodynamically favorable, but fully wetted states appeared to be kinetically trapped due to the strong cohesion of water and the necessity of breaking multiple hydrogen bonds all at the same time to form a cavity [13, 14].

The possibility of dewetting in membrane pores made it relevant to the mechanisms of hydrophobic gating in ion channels. Sansom and colleagues [15, 16] simulated different pores in model membranes and found a critical dependence of liquid water stability inside the pore on the radius of the pore and the presence of polar atoms in the lining. A classical thermodynamic description of vapor plug formation in ion channels and the possible role of hydrophobic gases displacing water from the gate was recently given by Roth and co-authors [17, 18].

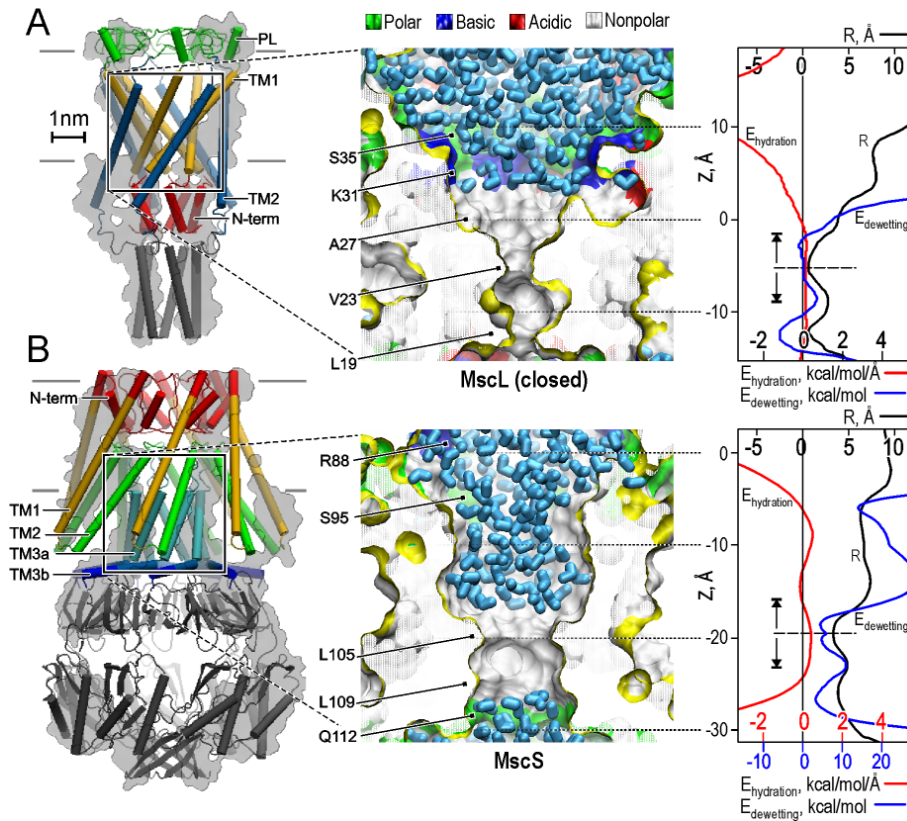


Figure 1. Hydrophobic gates in mechanosensitive MscL and MscS channels are dehydrated. (A) The closed-state model of *E. coli* MscL built by homology to the crystal structure of MscL from *Mycobacterium tuberculosis*. Color coding of MscL: N-terminal (red), TM1 (yellow), periplasmic loops (green) and TM2 (blue); (B) crystal structure of *E. coli* MscS supplemented with N-terminal domains (red) modeled *de novo* (see text). The MscS transmembrane region is color-coded as: N-terminal (red), TM1 (yellow), TM2 (green), TM3a (cyan) and TM3b (blue). Snapshots of MD simulations showing vapor-locked states of the channel gates (middle column). Graphs of internal radii, hydration energy and dewetting energy plotted as functions of z coordinate (pore axis). Dewetting energy for each half of the pore (above or below the constriction) was calculated as the difference between the energy of water–vapor interface at a given z location and the sum of water–protein interactions lost in the dehydration zone (see section 2).

As for the real channels of known structures, exclusion of water from the narrow hydrophobic constriction was suggested by the first MD simulations of the large-conductance mechanosensitive channel MscL [19]. A more substantial dewetting of the pore was observed in simulations of the crystal structure of the functionally similar, but structurally unrelated, small-conductance mechanosensitive channel MscS [20]. Subsequently, a similar behavior of water intermittently filling and vacating the gate was observed in MD simulations of the pentameric nicotinic acetylcholine receptor [21, 22]. The recent molecular dynamics study of the Kv1.2 channel clearly suggested dewetting of the inner cavity as the mechanism of K channel rectification [23].

Local evaporation of water in a hydrophobic constriction is different from occlusion of a fully hydrated pore by tightly packed sidechains of the protein, but how? A localized phase transition in the pore interrupts the continuous water column and leads to a formation of two water–vapor interfaces on both sides of the constriction. First, this makes the pore leak-proof, preventing accidental passages of inorganic ions and protons. Second, because the two interfaces bear surface tension which can be as high as 70 mN m^{-1} (17.7 kT nm^{-2}), they would additionally constrict and stabilize the narrow non-conductive

state of the pore. Third, the interfaces may not stay at the place where they formed initially but move out of the hydrophobic constriction to minimize their energy. In contrast to occlusion by sidechains attached to the protein backbone, the fluid phase has more freedom to rearrange and move the interfaces away from the reach of a thermal fluctuation, thus stably locking the non-conductive state. Opening of the channel will be opposed by tension at the interfaces until the pore is completely wet inside. As will be discussed below, this process may pose a rate-limiting barrier for the gating kinetics.

In the present work we consider gating of two bacterial mechanosensitive channels, MscL and MscS. Both channels serve as osmolyte release valves in bacterial cells and open directly by tension in the surrounding lipid bilayer [24]. The MscL channel was first isolated from *E. coli* [25] and its thermodynamic parameters and the spatial scale of the gating transition were determined in reconstituted liposomes [26] and in native membrane patches [27]. The crystal structure of MscL from *Mycobacterium tuberculosis* [28] revealed a pentamer of two-transmembrane domain subunits; the pore-lining TM1 bearing the gate and the lipid-exposed TM2 (figure 1(A)). The crystal structure served as a template for modeling of *E. coli* MscL whose functional properties were

better understood. Under tensions approaching the lytic threshold for the cytoplasmic membrane ($10\text{--}14\text{ mN m}^{-1}$), MscL opens a 3.2 nS non-selective pore acting as an emergency release valve. The opening pathway for MscL associated with iris-like motion transmembrane helices was proposed as a sequence of models [29] and supported by several low-resolution techniques [30–32].

E. coli MscS identified by homology to the K^+ -efflux channel KefA [33] was found to be a ubiquitous turgor regulator in bacteria and other walled cells [34]. Its crystal structure [35, 36] revealed a heptameric assembly of 3-transmembrane domain subunits with lipid-facing TM1–TM2 pairs, pore-lining TM3 helices and a hollow cytoplasmic domain (figure 1(B)). The structure was originally interpreted as an open state based on an un-occluded pore constriction $\sim 7\text{ \AA}$ in diameter [35]. MD simulations of the MscS transmembrane pore segment, however, revealed that the gate constriction is too hydrophobic and too narrow to be permanently hydrated and pass ions [20]. Similar conclusions were reached in independent simulations of the entire transmembrane domain of the channel with two different force fields [37, 38]. Importantly, the geometry of the crystal pore did not satisfy the experimental conductance of open MscS, while the attempts to make the TM3 barrel more narrow to occlude the lumen with sidechains resulted in conformations similar to the crystal one [39, 40], suggesting that the crystallographic state of the pore is one of the most compact. Membrane tension transmitted through the TM2–TM3 interhelical contacts is predicted to expand the MscS barrel by tilting and straightening the pore-lining helices and promote complete wetting [41–43]. The open pore maintains a bulk-like regime of ionic conduction, permitting passage of fully hydrated ions [42, 44]. The open state is stable for hundreds of milliseconds under moderate tensions of $5\text{--}7\text{ mN m}^{-1}$.

Below we discuss the opening processes of MscL and MscS that include a critical wetting step. We attempt visualization of the process of pore wetting using conventional equilibrium and steered molecular dynamics, which emphasized that wetting/dewetting transitions can occur on a nanosecond timescale, whereas the concerted motions of protein domains during gating transitions can be much slower. We find discrepancies between the simulated wetting events and experimentally predicted barrier positions on the pore expansion coordinate. We also perform analysis of pore surfaces and hydration energies in the macroscopic approximation and find that the character of the pore lining changes with expansion. We illustrate the specific role of conserved glycines in the two bacterial mechanosensitive channels that change their exposure in the course of the opening transition and have strong effects on the stability of conductive states.

2. Methods

One of the major challenges for computational studies of ion channel gating is the drastic difference between the timescales of protein conformational changes (microseconds to seconds)

and relaxation of the solvent, which can be of the order of nanoseconds. Since our focus here is primarily on hydration, simulations estimating the probability of the gate occupancy by water were performed essentially with the restrained protein backbone near the fully closed, open or intermediate conformations. To assess the hydration properties of the pore surface along the previously proposed opening pathways for MscL [45] and MscS [42], the backbone was relatively slowly driven from the resting to the fully open conformation allowing for local equilibration of water and side chains. Some intermediate conformations were additionally equilibrated to allow the unrestrained side chains to relax in the explicit medium so that the surface topology would allow for more realistic estimations of the exposed atomic areas. These areas were then taken for estimations of hydration energies using experimentally determined solvation parameters [46, 47].

2.1. Molecular dynamics simulations and analysis

All molecular dynamics (MD) simulations were carried out with NAMD (version 2.6) [48], utilizing the CHARMM 27 force field and either TIP3P or SPC water models. Simulations in equilibrium and steered (SMD) modes were set as an NPT ensemble at 310 K , under 1 atm . The particle-mesh Ewald [49] method for long-range electrostatics estimation was used with a 10 \AA cutoff for short-range electrostatic and van der Waals forces. Visualization of states, molecular modifications and analysis were done in VMD [50] using the embedded Tcl language, providing a flexible and convenient environment for analysis of trajectories.

In this study we utilized the models of *Escherichia coli* MscL [45] built on the template of MscL from *M. tuberculosis* [28]. The alignment of the two sequences can be found in [28]. The closed and open MscL models were equilibrated for 4 ns with a restrained backbone and then for 4 ns unrestrained in a fully hydrated POPC bilayer (306 lipids, 137 potassium and 137 chloride ions, $\sim 38\,000$ water molecules, $\sim 165\,000$ atoms in total) under 10 dyne cm^{-1} lateral tension. After that the protein structures were refined by symmetry-driven simulated annealing [51] in the same setting. To visualize the opening transition, a 10 ns steered simulation between the closed and open conformations was performed. A harmonic force was applied to the backbone of the residues located at the hydrophobic/hydrophilic interfaces of the POPC membrane (residues $17\text{--}21$ and $36\text{--}40$ on TM1 and $77\text{--}81$ and $97\text{--}101$ on TM2). The spring constant was dynamically adjusted every 1 ps in the range from 0.001 to $10\text{ kcal mol}^{-1}\text{ \AA}^{-2}$ to provide a nearly linear decrease in RMSD of the steered atoms from their target positions. Note that the timescale for the steered transition is much shorter than estimated in real experiments ($\sim 10\text{ }\mu\text{s}$) [52], but the simulation provides sufficient time for thermal relaxation of sidechains along the opening path. For the analysis of the hydration energy of the pore lumen during the gating transition, 18 intermediate frames were chosen from the steered trajectory and refined through symmetry-driven annealing in the same setting.

MscS crystal structure with added N-terminal domain was created using the crystallographic coordinates for residues 27–280 (PDB ID 2OAU) [36] and the coordinates of the first 26 amino acids from our published model [40]. The structure was energy-minimized with sevenfold rotational symmetry restraints embedded into the fully hydrated POPC bilayer (220 lipids, 53 potassium and 60 chloride ions, ~30 000 water molecules, ~150 000 atoms in total) and simulated for 12 ns at 10 dyne cm⁻¹ lateral tension. Since the crystal conformation of MscS with the splayed lipid-facing helices and unsupported TM3 pore barrel was shown to be prone to deformation and collapse of the gate region in unrestrained simulations [37], we have harmonically restrained the backbone near the starting position to estimate the hydration status of that conformation.

The steered transition between the closed [40] and open [42] models of MscS was performed over 4 ns using the same adaptive steering protocol as described above for MscL. All the backbone atoms of the transmembrane domain were steered towards the target. The conformation at ~30% of the transition was picked to illustrate the intermediate with the interhelical glycines starting to be exposed to water. The structure was refined with a 1 ns symmetry annealing [51] and used for calculation of the hydration energy profiles along with the closed and open conformations. Then in the above three structures glycines 101 and 104 were mutated to alanines using the PSFGEN plug-in to VMD, energy-minimized and used for estimation of the hydration energies of the G101A–G104A mutant.

Analysis of the solvent-exposed protein surface area was conducted with either GETAREA [53] and custom-written PDBAN software for MscL, or using a custom-written VMD script with the probe radius 1.77 Å (VdW radius of the TIP3P water model) for MscS. Solvation energy per atom was estimated utilizing commonly used solvation parameters [46]. Atoms exposed to the pore lumen were grouped into 1 Å slices normal to the pore axis and the total hydration energy was calculated for every slice. The resultant profile was smoothed by a twofold nearest-neighbor averaging (preserving the total hydration energy of the whole channel) approximating thermal fluctuations with an RMSD of ~1 Å.

The free energy of dewetting was calculated as the difference between the interfacial energy of newly created air–water boundaries and the energy of water–protein interactions lost due to water retraction from the segment of the pore [20]:

$$w_{dw}(z) = \sigma A_{wv}(z) - \int_{z_0}^z S_p(z) L_{wp}(z) dz$$

where $A_{wv}(z)$ is the area of water–vacuum interface (approximated with the cross-sectional area of the pore in a given location z), $S_p(z)$ is the protein hydration energy per square ångström, $L_{wp}(z)$ is the perimeter of the pore cross section. Surface tension σ at the water–vapor interface was assumed to be equal to the macroscopic value of 70 mN m⁻¹. However, in a nanoscale confinement the value of σ can be lower as suggested by MD simulations [5] and by spectroscopic measurements on water clusters [4] and water near hydrophobic surfaces [6].

2.2. Experimental procedures

Detailed descriptions of methods can be found in previous publications [27, 41, 54]. Briefly, MscL and MscS proteins were expressed in MJF465 *E. coli* cells [33] from pB10b-based vectors [55, 56]. Giant spheroplasts were generated as previously [54] and mechano-activated currents were recorded in excised patches under pressure ramps delivered from an HSPC-1 pressure-clamp machine (ALA Instruments). Analysis of traces involved series resistance compensation, current normalization and activation curve fitting, which was done using Clampfit (Molecular Devices) and Microsoft Excel. Dose–response curves were treated in a two-state Boltzmann approximation ($P_o/P_c = \exp[-(\Delta E - \gamma \Delta A)/kT]$), as described in section 3.2.

3. Results

3.1. The gates are stably dehydrated in the resting states of MscL and MscS

Figure 1 shows results of all-atom MD simulations of closed models of MscL and MscS channels in fully hydrated POPC bilayers with TIP3P water. Entire structures are shown on the left with horizontal lines delineating the membrane. Each of the structures was simulated for at least 12 ns. The gate segments are depicted in the middle with the protein shown as a solvent-accessible surface colored according to the type of amino acid lining the pore. In both instances the constrictions are extremely hydrophobic and not occluded completely by sidechains. The 3.5 Å MscL pore may accommodate a single string of water, whereas 2–3 strings of water fit in the gate of MscS, which is 6.5 Å wide. Under chosen simulation conditions, water was not detected inside the gate of MscL, but single, double and very rarely triple strings of water occupied the constriction of simulated MscS 26% of the time.

The graphs of hydration and dewetting energies in MscL and MscS are presented on the right side of figure 1. The red line represents the density of the protein surface hydration energy (E_{wp}) along the z coordinate calculated from the atomic areas exposed to the lumen and atomic solvation parameters [46]. The blue line is the dewetting (desolvation) (E_{dw}) free energy computed as the difference between the energy of the water–vapor boundary ($\sigma \pi r^2$) at a given radius of the pore (black line) and the sum of all protein–water interactions lost in the dehydrated zone. This calculation made with surface tension $\sigma = 70$ mN m⁻¹ is a result of an imaginary experiment when the continuous water column is broken at the constriction and the two water–vapor boundaries are moved apart. The minima of dewetting energy predict stable positions of the water–vapor boundary in each half of the pore.

In pentameric MscL, the gate is formed by five sidechains of L19 on the cytoplasmic side and five smaller V23 sidechains on the periplasmic side. The small residue above the constriction (A27) makes the pore wider and the E_{dw} (where $\sigma \pi r^2$ is the dominant term) sharply increases with the pore radius. The position of the upper boundary predicted from purely macroscopic considerations is very close to the

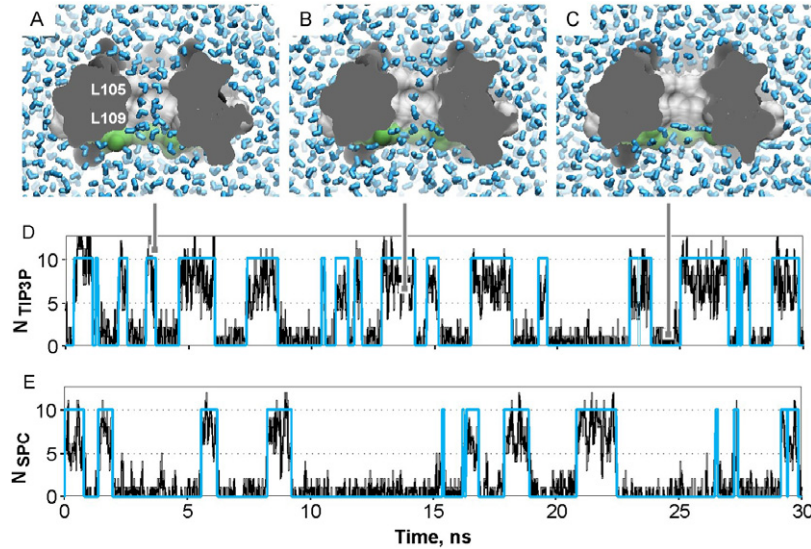


Figure 2. Molecular dynamics simulations of the ‘gate ring’ of MscS with two water models, TIP3P and SPC. The gate ring consisting of seven alpha-helices 11-residue long includes gate-keeping L105 and L109 (denoted in (A)). During simulations the backbone was softly restrained at the crystallographic positions. Simulated in isolation, the gate shows pronounced dewetting transitions. With TIP3P water, the ring displayed a double string of water inside $\sim 45\%$ of time (A), $\sim 15\%$ single string (B) and 40% of time it was completely dehydrated (C). The ring surrounded by rigid SPC water displayed completely dehydrated state $\sim 60\%$ of time. The water molecule count inside the ring in the course of 30 ns simulations is shown in panels (D) (TIP3P) and (E) (SPC). The kinetics of transitions shows that the lifetime of water strings is of the order of 1–3 ns. Note that the simulated gate conformation is estimated to be non-conductive for ions even when the water strings are present since this water way is too narrow to provide a hydration shell for the ion in the hydrophobic environment [15, 20].

constriction: however, in simulations, the average boundary position is 4–5 Å above the predicted minimum apparently due to the finite size of water molecules and some cooperativity of water–water interactions. In MscS, which is a homoheptamer, the constriction is lined by two rings of leucines (L105 and L109) and due to the packing constraints imposed by the sevenfold symmetry it cannot be as compact as in MscL. Interestingly the isolated gate represented by a small barrel formed by seven 11-residue helices including L105 and L109 undergoes similar desolvation when simulated in TIP3P and SPC water (figure 2). The time spent in the desolvated state clearly depends on the water model and with more advanced or polarizable water models one may expect substantial shifts in occupancy. We should note that the intermittent 1–3 ns wetting events should not be interpreted as openings, since even with water strings the hydrophobic pore is too narrow to conduct fully hydrated ions [20]. These fast wetting transitions may not be observed in channel configurations where the two water–vapor boundaries are further separated, such as in MscL (figure 1).

In MscS, the gate is not in the center of the transmembrane domain and so the access pathways (vestibules) are asymmetric, with a larger ‘outer chamber’ on the periplasmic side. Below the gate, the polar ring of Q112 defines the position of the minimum for E_{dw} , and immediately above the gate, E_{dw} shows its first minimum as well. The outer chamber lined by A98 and A102 is also hydrophobic, which generates a second minimum for $E_{dw} \sim 13$ Å above the gate [20] introducing some ambiguity in the position of the upper water boundary. We have preliminary data that hydrophilization of the outer chamber with A98S and A102S mutations strongly

changes the character of gating; it decreases the barrier and lowers the energy gap between the closed and open states. This suggests that in the resting state the outer chamber of MscS is likely to also be dehydrated and its wetting appears to be the first step toward opening. This problem will be addressed in a separate paper [71]. Irrespective of the resting position of the outer boundary, we may state that in both channels gates are strongly dehydrated and opening must be associated with a considerable expansion of the pore that would allow for complete wetting and aqueous passage for hydrated ions.

3.2. Spatial scales of tension-driven transitions

For each channel structure, the diameter of the open pore is related to the amount of total in-plane expansion of the transmembrane domain (ΔA) associated with the transition. Previously, the areal expansions were calculated from the slopes of activation (dose–response) curves for each channel. The conductances estimated for the open-state models constrained by ΔA were very close to those experimentally measured. The closed–open equilibrium constant ($K_{eq} = P_o/P_c$) for each channel is reasonably well described in the two-state Boltzmann approximation: $P_o/P_c = \exp[-(\Delta E - \gamma \Delta A)/kT]$, where P_o and P_c are the open-and closed-state probabilities, ΔE is the free energy difference between the states, ΔA is the in-plane protein expansion, γ is membrane tension, k is the Boltzmann constant and T is the absolute temperature. For high-threshold MscL, which opens at $\gamma \sim 10$ –14 mN m $^{-1}$ [26, 57], fitting of experimental $P_o(\gamma)$ curves estimates ΔE as about 50 kT for the transition associated with $\Delta A \sim 20$ nm 2 . This amount of barrel expansion opens a

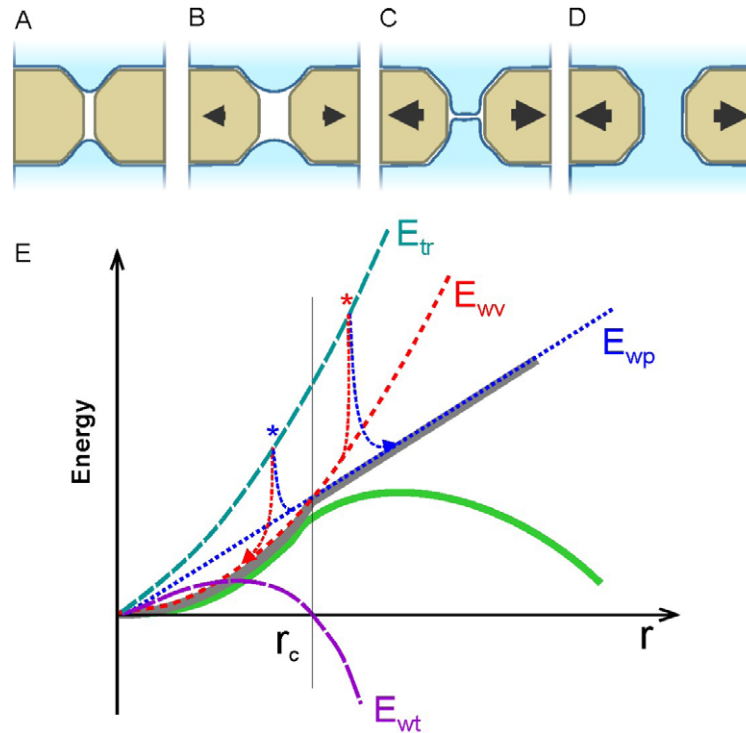


Figure 3. Wetting energetics of a hydrophobic pore. A sequence of pore conformations ((A)–(D)) in the course of expansion under lateral tension (black arrows). (A) A narrow dehydrated state of the pore; (B) expanded dehydrated pore; (C) transition state; (D) fully hydrated conductive state of the pore; (E) energies of different states as a function of pore radius. In configuration (A) the interfacial component of the free energy is represented only by the energy of the water–vapor interfaces (E_{wv} , red line). E_{wv} grows as the square of the pore radius $E_{wv} = 2\sigma_{wv}\pi r^2$, where σ_{wv} is the surface tension of water–vapor interface. The hydration energy of a fully hydrated pore grows linearly with the radius, $E_{wp} = 2\sigma_{wp}\pi r l$, where σ_{wp} is tension at the water–protein interface represented as a cylinder of radius r and length l . Purple line is wetting energy $E_{wt} = E_{wp} - E_{wv}$. Expansion beyond the critical radius (r_c) at which $E_{wt} = 0$ makes wetting thermodynamically favorable. The energy of the transition state (E_{tr}) with a narrow slit separating the two aqueous phases is roughly the sum of E_{wv} and E_{wp} . Switching between the dewetted and hydrated states in either direction should go through transition states denoted by asterisks (see text).

~ 3 nm non-selective pore which conducts at 3 nS in 200 mM KCl [27]. The MscS channel opens at tensions considerably lower than MscL (5.5 – 7.8 mN m $^{-1}$) and the transition takes less energy ($\Delta E \sim 20$ – 24 kT). The channel is predicted to expand by $\Delta A \sim 15$ nm 2 to open a pore ~ 1.6 nm in diameter conducting at 1.1 nS in a similar buffer [42, 54, 58].

3.3. The hydration energy profile for opening and closing of a generic hydrophobic pore

Having observed consistent dewetting of MscL and MscS gates, we turned to a simplified model of a hydrophobic pore. Consideration of interfacial energies associated with expansion of a pore may explain why dewetting can pose a barrier separating the two states and kinetically limits both opening and closing. Figures 3(A)–(D) depicts the evolution of a simple hydrophobic pore under lateral tension applied through the membrane. In the beginning, the pore is narrow and dehydrated, and the interfacial component of the free energy (E_w) is represented only by the energy of the water–vapor interfaces (E_{wv}), which grows as the square of the pore radius $E_{wv} = 2\sigma_{wv}\pi r^2$, where σ_{wv} is the surface tension of the water–vapor interface (red dashed line, panel (E)). When the pore is fully hydrated, the interfacial energy is expected to grow linearly with the radius, $E_{wp} = 2\sigma_{wp}\pi r l$, where σ_{wp}

is tension at the cylindrical water–protein interface of radius r and length l . The parabola describing expansion of the ‘dry’ pore intersects with the straight line of the wet pore energy at the critical radius of wetting (r_c). Expansion beyond this point makes the wetting event thermodynamically favorable as the wetting energy $E_{wt} = E_{wp} - E_{wv} - PV$ (purple line in panel (E)) becomes negative. The PV term acknowledges the work of ‘flooding’ the pore of volume V under atmospheric pressure P , but its value is estimated to be only ~ 0.1 – 0.2 kT. Neglecting the PV term, we can see that the condition $E_{wt} = E_{wp} - E_{wv} = 0$ sets the critical radius for wetting as $r_c = l\sigma_{wp}/\sigma_{wv}$. This gives a simple prediction that wetting will be more favorable and will occur at smaller radii when the pore is shorter and less hydrophobic, i.e. σ_{wp} is low.

To estimate the potential contribution of interfacial effects, we took the spatial and energetic scales of the MscL opening and related r_c with some realistic values of surface tensions, in the simplistic assumption that they are the only contributions to the transition energy. The wetting energy E_{wp} taken as 50 kT, which corresponds to the experimental transition energy for MscL [27], and typical values of $l = 2$ nm, $\sigma_{wv} = 70$ mN m $^{-1}$ and $\sigma_{wp} = 20$ mN m $^{-1}$ produce $r_c = 0.5$ nm. The tension at the protein–water interface taken for this calculation is about two times higher than the value derived from the typical solvation energies of water-exposed aliphatic protein groups

reported to be $0.012\text{--}0.014\text{ kcal mol}^{-1}\text{ \AA}^{-2}$ [46, 47], or about 10 mN m^{-1} . Based on this σ_{wp} estimate for an idealized hydrophobic pore, one can see that the surface term can be significant and comparable with the sum of other energy terms associated with the expansion of a real protein.

As has been noted [14], the thermodynamic possibility of a wetting or dewetting transition does not ensure fast equilibration since the two states can be separated by a kinetic barrier. Figure 3(C) depicts the possible transition state where the upper and lower aqueous reservoirs are still separated by a thin gap of gaseous phase. This configuration is close to the complete wetting, yet it is energetically most costly because the water–vapor interfaces still exist and at the same time water hydrates most of the hydrophobic surface. The interfacial energy of this transition state would be roughly the sum of the energies for the fully wetted and dehydrated states ($E_{\text{tr}} = E_{\text{wp}} + E_{\text{wv}}$) as depicted by the dashed parabola (dark green) passing above. Note that a similar transition state may be inferred for the processes in both directions, for the opening (wetting) as well as for the closing process when the water column has to be interrupted by severing many hydrogen bonds all at the same time. If we follow expansion along the ‘dry’ pore parabola (red) and pass the intersection with the ‘wet’ pore line, we will be in the regime where wetting is thermodynamically preferable, but the system must wait for a fluctuation and reach the transition state in order to switch the regime. Following the opposite direction, a constricting water-filled pore would also require a fluctuation that would disrupt the continuous water column, but likely in a different spot of the trajectory, at a smaller radius. When the tension stimulus is dynamic, the two transition barriers, on the way up and on the way down, may be different and the system may feature unequal radius/tension dependences for the opening and closing rates, generally implying hysteresis. Hysteresis in wetting–dewetting processes has been previously studied experimentally and simulated in different systems [59, 60] and is observed with MscS (see below).

One should note that, although wetting/dewetting transitions imply the presence of a barrier, irrespective of the wetting state the energy of the system grows monotonically with pore expansion and thus wider states (in this approximation) are principally less stable than the narrow states. In the absence of tension the pore will always close. Yet, phenomenologically, the conductive states in MscL, and especially in MscS, are stable for tens or hundreds of milliseconds when measured at a threshold tension and feature well-defined single-channel conductances that do not change visibly with tension. This implies that there is an additional mechanism stabilizing the geometry of the open pore. One obvious way to stabilize a conductive state is to decrease tension at the protein–water interface which can be achieved through exposure of a few polar groups to the lumen of the pore in the course of expansion. This would bend the energy profile down as shown in figure 3(E) (green line) favoring open conformations. Note that the graph shows only the energy of pore hydration while a more realistic profile involving other energy contributions from protein conformation, protein–lipid interactions [61, 62], distortion of surrounding lipids [63, 64],

etc, would be represented by two wells and the steeply growing energy with radius beyond the open well that should structurally limit protein expansion. The analysis of pore expansion in both MscL and MscS presented below shows that this process indeed opens water access to polar atoms, making the pore surface more hydrophilic and experiments indicate that the associated change of hydration energy substantially contributes to the overall energy profile.

3.4. An attempt to observe critical wetting event in MD simulations of MscL

We returned back to a realistic model of the MscL channel to perform a simulation that would let us observe the pore opening event and determine the critical radius of wetting. The iris-like transition in MscL was proposed through computational modeling [45], in which the pairs of TM1 and TM2 helices gradually tilt and move outward, opening a 3 nm pore. TM1 helices primarily line the pore. MD simulations suggested a similar character of helical motions [19], and this character of transition was experimentally supported by disulfide crosslinks [30], site-directed spin labeling and EPR studies [31] as well as by FRET experiments [32].

The previously published resting state and the open-state MscL models [40, 42] were equilibrated in a fully hydrated POPC bilayer for 4 ns. The transition was envisioned with a relatively slow (10 ns) steering of the closed model toward the open one. To imitate the lateral pressure/tension profile in a POPC membrane, the steering force was applied only to the backbone of the residues on the TM1 and TM2 ends at the hydrophobic/hydrophilic interfaces of the lipids (residues 17–21 and 36–40 on TM1 and 77–81 and 97–101 on TM2). The snapshots of a near-resting dehydrated state and of an intermediate (50% open) state with uniform wetting are shown as cross sections in figures 4(A) and (B), respectively. Utilizing a custom-written feedback protocol, the harmonic force driving the initial structure towards the attractor state was frequently adjusted to achieve a linear decrease of RMSD between the steered model and the target with time (figure 4(C), black line). The average total force applied to the channel driving the transition (green trajectory) increases steeply within the first 2 ns, passes through a shallow maximum and then remains nearly constant for the rest of the simulation, increasing slightly towards the end. The blue trajectory represents water occupancy inside the pore constriction (within a 5 Å slab between the average z positions of the L19 and V23 alpha-carbons). The number of waters stays near zero (point A corresponding to the conformation in panel (A)) for the first nanosecond and then, surprisingly, grows gradually, having no difficulty wetting the expanding walls of the channel as if they are hydrophilic. There are no visible water–vapor boundaries in the system configuration beyond the second nanosecond, and no sharp wetting transition.

It seems reasonable to expect that overcoming the wetting barrier should coincide with the maximum force. The first maximum near the 2 ns point indeed corresponds to the configuration of water just prior to the complete merging of the upper and lower water phases. Molecular dynamics of MscL with TIP3P water and the CHARMM force field

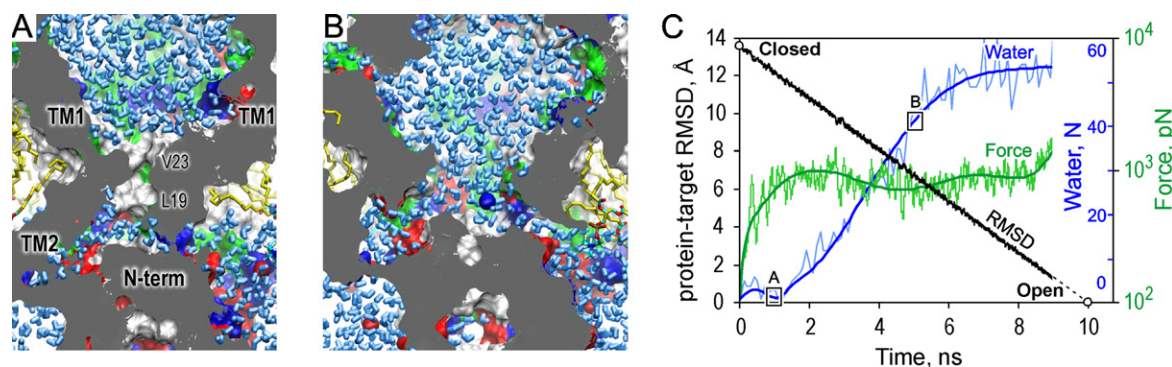


Figure 4. The results of steered MD simulation of *E. coli* MscL with TIP3P water. MscL was slowly driven between its pre-equilibrated resting and open states. (A) Cross section of the resting pore; (B) is the pre-expanded state halfway to the open state; (C) the trajectories of RMSD change (black line), steering force (green) and the number of water molecules in the constriction in the course of expansion. Note that wetting occurs early, without a sharp transition.

thus predicts an easy and early wettability of the pore. As a result, the observed position of the hydration barrier (transition state) at 0.2 on the RMSD reaction coordinate in this simulation does not correspond to the main transition barrier near 0.67 on the protein expansion coordinate, which was predicted from the results of kinetic [26] and substate occupancy [65] analyses. Computation of hydration energies in the constriction from solvation parameters presented below suggests that the hydration energy barrier of the MscL pore can be between 0.6 and 0.7 of the full expansion.

3.5. The character of pore lining changes from hydrophobic to hydrophilic during iris-like opening of MscL: ‘macroscopic’ estimations and experimental results

Utilizing the steered trajectory from the closed to open state described above, we chose 18 additional intermediate frames. We have refined these conformations using the symmetry annealing procedure [51] and analyzed hydration energy profiles inside the pore using GETAREA. The three conformations illustrating the iris-like barrel expansion and densities of hydration energy calculated for the central region of the pore ($-11 \text{ \AA} < z < 3 \text{ \AA}$, yellow strip) are shown in figures 5(A) and (B) and the cross sections of the constriction are rendered with solvent-accessible surfaces in panel (C). The surfaces illustrate substantial exposure of conserved glycines 22, 26, 30 and 34 in the intermediate and open states. The narrow closed pore is both hydrophobic and barely accessible to the solvent and for this reason the density of hydration energy is close to zero (panel (B), red line). The intermediate, 65% expanded state shows a negative and a positive peak, the latter signifying that the narrow part of the pore ($z = -6 \text{ \AA}$) remains partially hydrophobic (green line). Full expansion makes the entire pore substantially more hydrophilic (blue line). Integrals of hydration energy density in that range of z for 20 sequential conformations plotted against the effective in-plane area of the transmembrane barrel (figure 5(D)) indicate that the hydration energy shallowly increases with area, reaching its maximum near $\Delta A = 12 \text{ nm}^2$ (60% expanded state) and then drops more sharply due to exposure of the glycines. The slope of hydration energy with

expansion is the disjoining pressure that assists opening as the pore becomes more hydrophilic. The peak of disjoining hydration pressure in the middle of the transition attributable to glycines 22 and 26 and acting on the 10 \AA ring from inside is estimated as $\sim 270 \text{ atm}$. Exposure of these two residues stabilizes the fully open state by -6 kcal mol^{-1} .

Previous analysis of tension dependences of opening and closing rate constants indicated that the main kinetic barrier is near 67% on the expansion coordinate toward the open state [26]. Another study has shown that this barrier in fact leads to the low-conducting substate ($S_{0.13}$), which then resolves to the fully open state almost with no additional energetic expense [65]. The reconstructed energy profiles for WT MscL, the mild gain-of-function mutant V23T and the severe gain-of-function mutant V23D taken from [65] are presented in figure 5(E) in the same expansion scale as figure 5(D). For WT MscL, the main barrier essentially coincides with the breaking point of the hydration energy plot. Consistent with the reduction of the transition barrier, single-channel traces of three hydrophilic pore mutants (V23T, V23D and G22N, figure 1 in [65]) illustrate dramatically decreased lifetimes for the closed and open states compared to WT MscL. Both opening and closing rates for WT and the ‘mild’ V23T mutant differ by 2–3 orders of magnitude (figure 6 in the same publication).

Gain-of-function mutations (V23T and V23D) make the constriction increasingly more hydrophilic and the channel opens easily at progressively lower tension. The activation midpoints for the rate-limiting transitions (C–O or C– $S_{0.13}$) [65] are shown in figure 5(F) relative to WT MscL. Importantly, replacement of the single glycine 22 with a residue having a hydrophobic side chain covering the backbone (alanine or isoleucine) drastically increases the activation midpoint. Remarkably the small apolar side chain of Ala produces the largest shift of the activation curve to the right, apparently because it effectively excludes water from interacting with the backbone in position 22, but at the same time it does not perturb the overall packing of the inner helices hiding other glycines. Bulky isoleucine, in contrast, does not pack well in the crevice and may expose other polar groups such as G26, thus ‘undoing’ part of its own closed-state

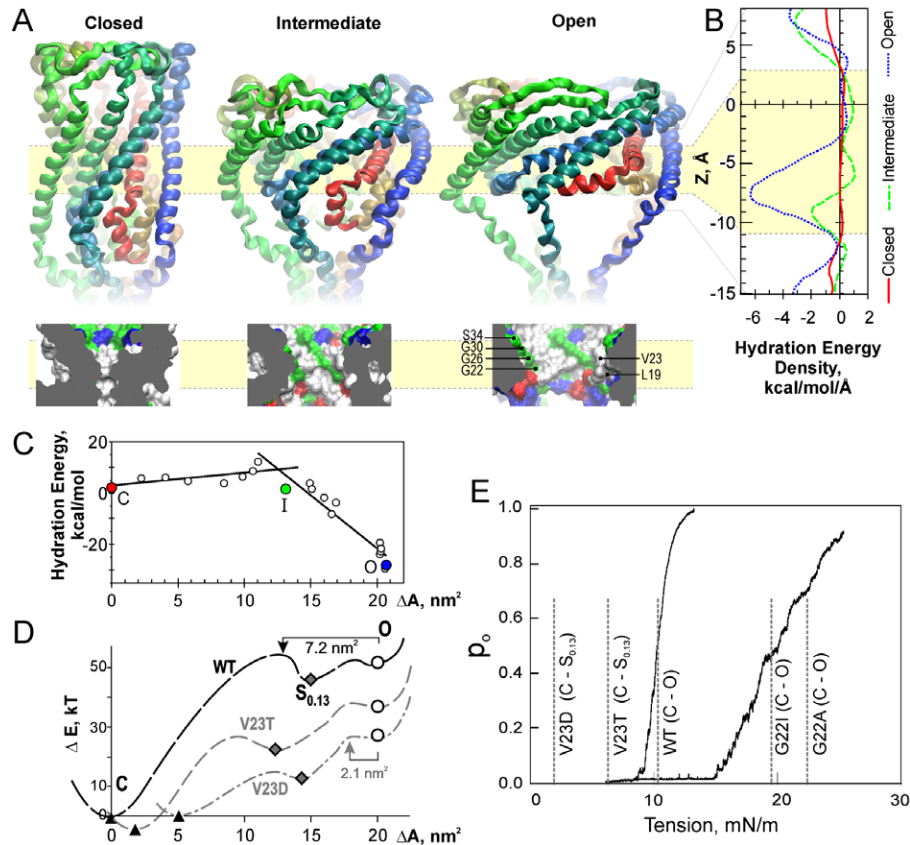


Figure 5. Changes of the pore hydration energy with expansion of MscL: macroscopic estimations and experimental results. (A) Three representative conformations of MscL: closed, intermediate and fully open. Yellow strip represents the central region of the pore ($-11 \text{ \AA} > z > 3 \text{ \AA}$) for which the densities of solvation energy were calculated. (B) Densities of hydration energy in the highlighted region for the three conformations calculated using GETAREA and atomic solvation parameters (see section 2). (C) Cross sections of the gate region illustrating gradual exposure of conserved glycines G22, G26, G30 and G34. (D) Solvation energies integrated over the central region in a series of conformations plotted as a function of in-plane area of the protein. Exposure of the glycines, which occurs near $\Delta A \sim 12 \text{ nm}^2$, sharply decreases the solvation energy. (E) Results of kinetic [26] and substate occupancy and analyses [65] predict the position of the rate-limiting barrier for the opening of wild-type (WT) MscL near 13 nm^2 on the ΔA coordinate. The main barrier is positioned between the fully closed state and the low-conducting substate $S_{0.13}$. Hydrophilic substitutions in the pore, V23D and V23T strongly decrease the barrier (data from [65]). (F) Activation curves for WT and G22I MscL. Vertical dashed lines represent the positions of activation curves for these and other mutants taken from [65, 66]. Alanine and isoleucine substitutions for G22 (G22I and G22A) strongly increase the midpoint tension for MscL activation.

stabilizing effect. Glycine 22 was recognized as the key residue defining the threshold for MscL activation and the full account of channel phenotypes with every substitution for G22 can be found in [66].

3.6. The opening pathway for MscS: the role of buried glycines in TM3

The opening pathway for MscS was recently predicted using the ‘extrapolated motion’ technique designed to model large-scale transitions [40, 42]. It permitted us first to modify the delipidated (splayed) crystal conformation and generate a compact model for the resting state with the lipid-exposed TM1–TM2 pairs attached to the inner TM3 barrel, and with the closed gate due to the presence of kinks in the pore-lining TM3s [40]. The second step was the exploration of expansion pathways and finding the most probable open states that would satisfy both the conductance and in-plane expansion of the transmembrane barrel [42]. The resultant transition

proceeded through simultaneous tilting and straightening of the transmembrane TM3 helices, which was largely confirmed by spin labeling and EPR techniques [43]. With the C-terminal ends of the kinked TM3 helices residing at the top of the cytoplasmic cage and separated by 54 \AA (measured between $C\alpha$ of the opposing F127), the extrapolated expansion of the transmembrane domain lead to the straightening of the kinks, tilting and outward motion of the central segments of TM3s that separated the gate [41, 42]. The extrapolated models for the closed and open states were refined using MD simulations and symmetry annealings in the explicit medium [51], and then the transition between the models was MD simulated in an all-atom setting in a slow (4 ns) steering mode to visualize the continuous expansion pathway.

The outer chamber, serving as a hydrophobic vestibule to the gate, is lined primarily by the sidechains of A98 and A102. This arrangement of TM3 helices is achieved through tight packing of G101 against A103 and G104 against A106 in a knob-into-hole manner [35, 39]. This makes the

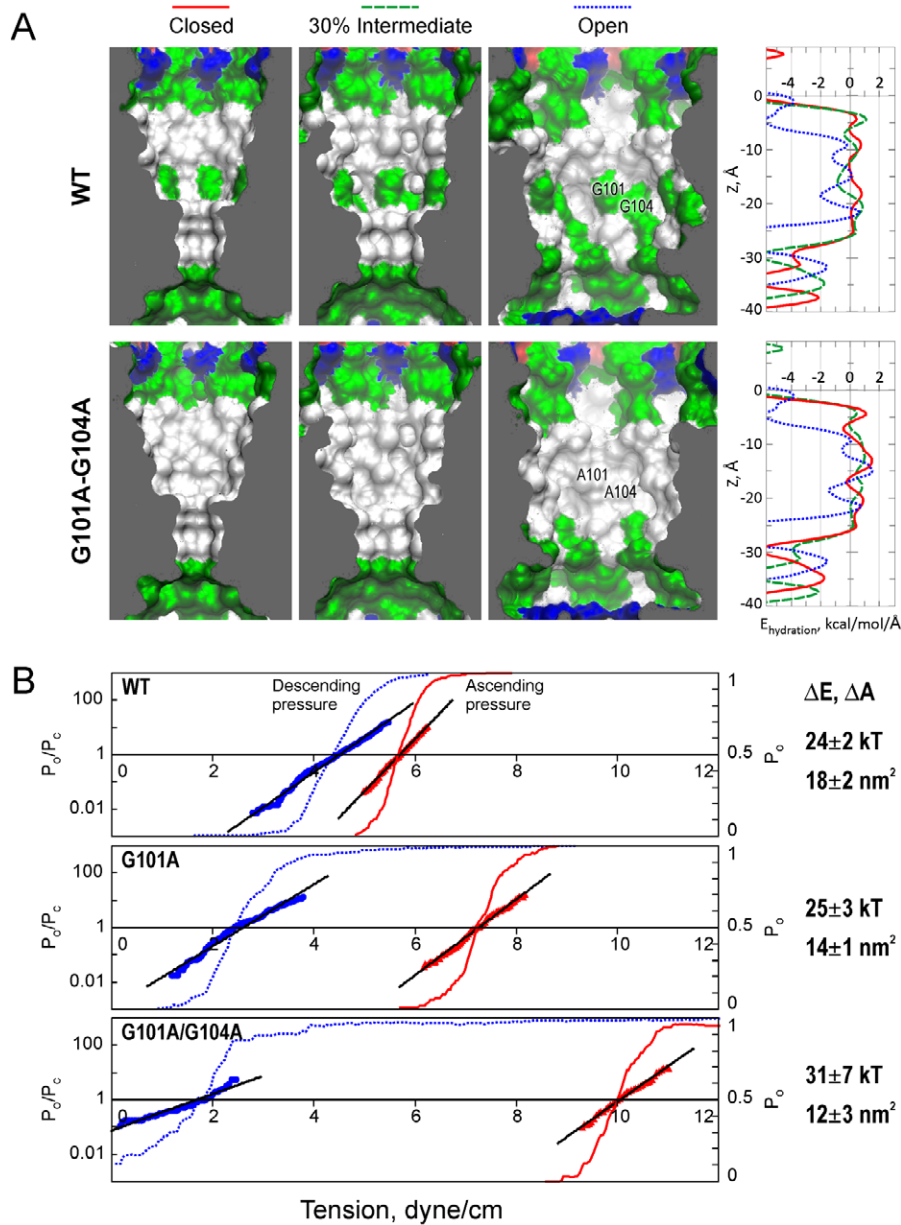


Figure 6. Expansion of the MscS barrel increases pore hydrophilicity through exposure of G101 and G104. (A) Snapshots of pore cross sections in the closed, 30% expanded and fully open states for WT (upper row) and G101A–G104A MscS (bottom row). The solvent-accessible surface of the pore is colored according to the type of residue: apolar (white), polar (green), positively charged (dark blue) or negatively charged (red). The alanine mutant pore shows no polar groups exposed in the closed and intermediate states. The hydration energy density graphs (panel (A), right side) show that moderate expansions result in a lower energy for WT. Hydration energy profiles are shown with a continuous red line for the closed state, dashed green line for the intermediate and dotted blue line for the open state. (B) Alanine substitutions for G101 and G104 progressively decrease tension sensitivity of the channel and increase hysteresis. These experimental traces were recorded in patches excised from giant spheroplasts under triangular ramps of pressure. Red traces represent responses to the ascending leg of the ramp (1 s long, from zero to saturation), while blue traces are responses to the descending ramp of the same speed. The results are represented as a normalized conductance (s-shaped P_o curve, right axis) and as a plot of $\ln(P_o/P_c)$ (left axis). Boltzmann fit of the linear region of the $\ln(P_o/P_c)$ produces estimates for ΔE and ΔA for the opening transition; the numbers presented on the right side correspond to the ascending ramp stimulus.

backbone of G101 and G104 only slightly visible from the lumen (figure 6(A)). A moderate (30%) expansion toward the open state well exposes G101 and G104 as is evident from the hydration energy density plot (figure 6(A), right side, green line). Further expansion to the fully open state is associated with a 53° clockwise rotation of TM3s [42], which exposes

the glycines more and makes the pore progressively more hydrophilic. This change of the character of the lining is predicted to alleviate the hydrophobic penalty of the open state. The cross sections of the G101A/G104A mutant pore (figure 6(A), bottom row), in contrast, indicate no exposure of the backbone in the closed and intermediate states and only

partial in the fully open conformation. The hydration energy of the G101A/G104A pore in the closed and intermediate states remains considerably more positive compared to WT.

Figure 6(B) illustrates the effects of G101A and G101A/G104A substitutions on the positions of activation curves measured in patch-clamp experiments under triangular pressure ramps. The ascending linear 1 s ramp from zero to saturating pressure was applied to an excised patch, which gradually opened the entire channel population. The responses in the forward direction are shown by red traces. Upon saturating the patch current, pressure linearly decreased with the same rate and the descending ramp response was recorded (blue trace). The pressure scale was converted into a tension scale with the assumption that in the forward direction the activation midpoint ($\gamma_{1/2}$) for WT MscS is 5.5 mN m^{-1} [44]. The activation data are presented in two forms; as raw $P_o(\gamma)$ curves and as linearized $\ln(P_o/P_c)$ plots; fitting of the latter with the two-state Boltzmann equation produced estimates for ΔE and ΔA shown on the right side of the graph. WT activates in the forward direction at moderate tension, but the closing follows a different trajectory with the lower midpoint, displaying a visible hysteresis. This hysteresis is of kinetic nature as responses to slower (30 s) ramps show practically no hysteresis. The single G101A substitution and the double mutation G101A–G104A progressively decrease tension sensitivity by shifting the activation midpoint in the forward direction to the right. At the same time, the midpoint for the closing process shifts to the left, making hysteresis stronger. The right shift of the activation curve with alanine substitutions can be easily explained by increased hydrophobicity of the pore throughout the transition. Indeed, in WT, a moderate expansion should produce polar groups and promote wetting of the outer chamber. The partially exposed G101 and G104 may try to maximize their interaction with water and this would facilitate TM3 rotation that would expose the glycines completely. The covered backbone in the alanine mutants implies that wetting of the pore would occur at much larger radii (see section 3.3) and thus the entire process would have to proceed over a higher barrier, as can be deduced from the diagram in figure 3. With a higher barrier and slow kinetics in both directions, the channel may resist opening until tension becomes high enough. Trapped in the open state beyond the barrier, the channel would exhibit delayed closure and a strong hysteresis. Importantly, hydrophilic substitutions A98S and A102S, which make the hydration of the outer chamber above the gate more stable, produce an opposite effect. They shift the activation curves to lower tensions signifying a decrease of total transition energy, increase the closing rates by 2–3 orders of magnitude and completely remove hysteresis [71].

The reversibility of opening/closing transitions in MscS and the nature of hysteresis should be further explored, and there are other factors to consider. Besides interfacial energies one should take into account flexibilities of TM3 helices which act as collapsible struts for the open frame of the channel. Indeed, previously, the double alanine substitution for G113 and G121 produced a channel that could be trapped in the open state for a few minutes without tension [41]. The stable open state was attributed to the absence of hinges in TM3 necessary

for helix buckling. The increased helical propensity in the double G101A–G104A mutant may contribute to the increase of the barrier when the channel attempts to exit the open state.

4. Conclusions

In the present work we combined molecular dynamics and structure-based macroscopic estimations with experimental analysis of gating of two bacterial mechanosensitive channels, MscL and MscS. Molecular simulations consistently show a dewetted (vapor-locked) state of channel gates. This makes the pore completely impermeable for inorganic ions and protons, and since the two water–vapor interfaces may bear surface tension up to 70 mN m^{-1} (17.7 kT nm^{-2}), they are predicted to additionally constrict and stabilize the narrow (non-conductive) state of the pore. Opening will be opposed by tension at the interfaces until the pore is completely wet inside. The dewetted (closed) and fully wetted (open) states are thus predicted to be separated by a barrier caused by unfavorable wetting of the pore. Increased wettability of the pore by hydrophilic substitutions decreases the energy of gating transitions and reduces the barrier between the states, based on tension midpoints and kinetics. Hydrophobic substitutions in the pore do the opposite. While other factors such as conformational energy of the protein itself, protein–lipid interactions [57, 62, 67] and elastic energy of distorted annular lipids [64, 68] should be considered, tension at water–vapor and hydrophobic protein surfaces clearly has a substantial contribution.

We need to be cautious about the value of surface tension for confined water. It has been suggested that the strength of hydrogen bonds in small clusters or in confined water is less than that in the bulk [4–6] and for this reason interfacial tension in confinement can be less than the macroscopically measured value. As water retracts from the narrow pore it may regain bulk-like properties and the increased tension may additionally stabilize the dewetted state of the pore.

The absence of a sharp wetting transition in MD simulations of MscL is likely a consequence of simple (although computationally effective) three-point water models and the non-polarizable force field we used. Lower cooperativity and directionality of hydrogen bond formation in the fixed-charge three-point TIP3P or SPC water than in real water may be the reason for easy wettability of pores lined by apolar sidechains. Indeed, the water–water and water–protein interactions in the CHARMM force field were parameterized for bulk and surface interactions but not for narrow confinement. Macroscopic estimations based on MD-derived exposed areas with experimental solvation parameters appear to be a way to circumvent some imperfectness of conventional force fields.

The change of the character of the pore lining in the course of expansion in both MscL and MscS is clearly attributable to the gradual exposure of polar groups. Patterns of highly conserved glycines typically lining one side of the pore-lining helix had been recognized as a factor that mediates tight helical packing in the resting state [39, 69, 70]. Here we show that the same glycines become exposed with pore expansion and

their favorable hydration creates disjoining pressure that assists opening.

Acknowledgments

The work was supported by NIH R01GM075225 and 2R01NS03931405A grants to SS.

References

- [1] Pomeau Y and Villiermaux E 2006 *Phys. Today* **59** 39
- [2] de Gennes P-G, Brochard-Wyart F and Quere D 2003 *Capillary and Wetting Phenomena. Drops, Bubbles, Pearls, Waves* (Berlin: Springer)
- [3] Chandler D 2005 *Nature* **437** 640
- [4] Luck W A P 1998 *J. Mol. Struct.* **448** 131
- [5] Di Leo J M and Maranon J 2003 *J. Mol. Struct. Theochem.* **623** 159
- [6] Scatena L F, Brown M G and Richmond G L 2001 *Science* **292** 908
- [7] Ball P 2008 *ChemPhysChem* **9** 2677
- [8] Lum K, Chandler D and Weeks J D 1999 *J. Phys. Chem. B* **103** 4570
- [9] Maccarini M *et al* 2007 *Langmuir* **23** 598
- [10] Steitz R *et al* 2003 *Langmuir* **19** 2409
- [11] Luzar A and Leung K 2000 *J. Chem. Phys.* **113** 5836
- [12] Hummer G, Rasaiah J C and Noworyta J P 2001 *Nature* **414** 188
- [13] Leung K, Luzar A and Bratko D 2003 *Phys. Rev. Lett.* **90** 065502
- [14] Leung K and Luzar A 2000 *J. Chem. Phys.* **113** 5845
- [15] Beckstein O and Sansom M S 2003 *Proc. Natl Acad. Sci. USA* **100** 7063
- [16] Beckstein O, Biggin P C and Sansom M S P 2001 *J. Phys. Chem. B* **105** 12902
- [17] Roth R and Kroll K M 2006 *J. Phys.: Condens. Matter* **18** 6517
- [18] Roth R, Gillespie D, Nonner W and Eisenberg R E 2008 *Biophys. J.* **94** 4282
- [19] Gullingsrud J, Kosztin D and Schulten K 2001 *Biophys. J.* **80** 2074
- [20] Anishkin A and Sukharev S 2004 *Biophys. J.* **86** 2883
- [21] Corry B 2006 *Biophys. J.* **90** 799
- [22] Beckstein O and Sansom M S 2006 *Phys. Biol.* **3** 147
- [23] Jensen M O *et al* 2010 *Proc. Natl Acad. Sci. USA* **107** 5833
- [24] Sukharev S I, Martinac B, Arshavsky V Y and Kung C 1993 *Biophys. J.* **65** 177
- [25] Sukharev S I, Blount P, Martinac B, Blattner F R and Kung C 1994 *Nature* **368** 265
- [26] Sukharev S I, Sigurdson W J, Kung C and Sachs F 1999 *J. Gen. Physiol.* **113** 525
- [27] Chiang C S, Anishkin A and Sukharev S 2004 *Biophys. J.* **86** 2846
- [28] Chang G, Spencer R H, Lee A T, Barclay M T and Rees D C 1998 *Science* **282** 2220
- [29] Sukharev S, Betanzos M, Chiang C S and Guy H R 2001 *Nature* **409** 720
- [30] Betanzos M, Chiang C S, Guy H R and Sukharev S 2002 *Nat. Struct. Biol.* **9** 704
- [31] Perozo E, Cortes D M, Sompornpisut P, Kloda A and Martinac B 2002 *Nature* **418** 942
- [32] Corry B, Rigby P, Liu Z W and Martinac B 2005 *Biophys. J.* **89** L49–51
- [33] Levina N, Totemeyer S, Stokes N R, Louis P, Jones M A and Booth I R 1999 *EMBO J.* **18** 1730
- [34] Pivetti C D *et al* 2003 *Microbiol. Mol. Biol. Rev.* **67** 66 table
- [35] Bass R B, Strop P, Barclay M and Rees D C 2002 *Science* **298** 1582
- [36] Steinbacher S, Bass R, Strop P and Rees D C 2007 *Mechanosensitive Ion Channels, Part A* vol 58 *Current Topics in Membranes* (New York: Elsevier) p 1
- [37] Sotomayor M and Schulten K 2004 *Biophys. J.* **87** 3050
- [38] Spronk S A, Elmore D E and Dougherty D A 2006 *Biophys. J.* **90** 3555
- [39] Edwards M D *et al* 2005 *Nat. Struct. Mol. Biol.* **12** 113
- [40] Anishkin A, Akitake B and Sukharev S 2008 *Biophys. J.* **94** 1252
- [41] Akitake B, Anishkin A, Liu N and Sukharev S 2007 *Nat. Struct. Mol. Biol.* **14** 1141
- [42] Anishkin A, Kamaraju K and Sukharev S 2008 *J. Gen. Physiol.* **132** 67
- [43] Vasquez V, Sotomayor M, Cordero-Morales J, Schulten K and Perozo E 2008 *Science* **321** 1210
- [44] Sukharev S 2002 *Biophys. J.* **83** 290
- [45] Sukharev S, Durell S R and Guy H R 2001 *Biophys. J.* **81** 917
- [46] Wesson L and Eisenberg D 1992 *Protein Sci.* **1** 227
- [47] Makhataдзе G I and Privalov P L 1995 *Adv. Protein Chem.* **47** 307
- [48] Phillips J C *et al* 2005 *J. Comput. Chem.* **26** 1781
- [49] Darden T, York D and Pedersen L 1993 *J. Chem. Phys.* **98** 10089
- [50] Humphrey W, Dalke A and Schulten K 1996 *J. Mol. Graph.* **14** 33
- [51] Anishkin A, Milac A L and Guy H R 2010 *Proteins* **78** 932
- [52] Shapovalov G and Lester H A 2004 *J. Gen. Physiol.* **124** 151
- [53] Fraczekiewicz R and Braun W 1998 *J. Comput. Chem.* **19** 319–33
- [54] Akitake B, Anishkin A and Sukharev S 2005 *J. Gen. Physiol.* **125** 143
- [55] Blount P, Sukharev S I, Moe P C, Schroeder M J, Guy H R and Kung C 1996 *EMBO J.* **15** 4798
- [56] Okada K, Moe P C and Blount P 2002 *J. Biol. Chem.* **277** 27682
- [57] Moe P and Blount P 2005 *Biochemistry* **44** 12239
- [58] Belyy V, Kamaraju K, Akitake B, Anishkin A and Sukharev S 2010 *J. Gen. Physiol.* **135** 641
- [59] Chen Y L, Helm C A and Israelachvili J N 1991 *J. Phys. Chem.* **95** 10736
- [60] Jin W, Koplik J and Banavar J R 1997 *Phys. Rev. Lett.* **78** 1520
- [61] Chiang C S, Shirinian L and Sukharev S 2005 *Biochemistry* **44** 12589
- [62] Marsh D 2008 *Biochim. Biophys. Acta* **1778** 1545
- [63] Lundbaek J A, Birn P, Girshman J, Hansen A J and Andersen O S 1996 *Biochemistry* **35** 3825
- [64] Wiggins P and Phillips R 2005 *Biophys. J.* **88** 880
- [65] Anishkin A, Chiang C S and Sukharev S 2005 *J. Gen. Physiol.* **125** 155
- [66] Yoshimura K, Batiza A, Schroeder M, Blount P and Kung C 1999 *Biophys. J.* **77** 1960
- [67] White S H and Wimley W C 1999 *Annu. Rev. Biophys. Biomol. Struct.* **28** 319
- [68] Nielsen C and Andersen O S 2000 *Biophys. J.* **79** 2583
- [69] Bowie J U 1997 *J. Mol. Biol.* **272** 780
- [70] Ou X, Blount P, Hoffman R J and Kung C 1998 *Proc. Natl Acad. Sci. USA* **95** 11471
- [71] Anishkin A *et al* in preparation